Constraining chameleon screening using galaxy cluster dynamics

Yacer Boumechta,[1,2,3,4,*] Balakrishna S. Haridasu ,[1,4,3,†] Lorenzo Pizzuti ,[5,‡] Minahil Adil Butt,[1,3,4,§]
Carlo Baccigalupi ,[1,3,4,‖] and Andrea Lapi[1,3,4,6,¶]

[1]*SISSA-International School for Advanced Studies, Via Bonomea 265, 34136 Trieste, Italy*
[2]*ICTP-The Abdus Salam International Centre for Theoretical Physics, Strada Costiera 11, 34151 Trieste, Italy*
[3]*IFPU, Institute for Fundamental Physics of the Universe, via Beirut 2, 34151 Trieste, Italy*
[4]*INFN, Sezione di Trieste, Via Valerio 2, I-34127 Trieste, Italy*
[5]*CEICO, Institute of Physics of the Czech Academy of Sciences, Na Slovance 2, 182 21 Praha 8, Czechia*
[6]*IRA-INAF, Via Gobetti 101, 40129 Bologna, Italy*

We constrain the chameleon screening mechanism in galaxy clusters, essentially obtaining limits on the coupling strength β and the asymptotic value of the field ϕ_∞. For this purpose, we utilized a collection of the nine relaxed galaxy clusters within the X-COP compilation in the redshift range of $z \leq 0.1$. We implement the formalism assuming a Navarro-Frenk-White mass profile for the dark matter density and study the degeneracy present between the mass M_{500} and the chameleon coupling with a high degree of improvement in the constraints for excluded parameter space. We recast our constrain to an upper limit on the scalaron field in $f(R)$ subclass of models of $|f_{R0}| \leq 9.2 \times 10^{-6}$, using all the nine clusters and $|f_{R0}| \leq 1.2 \times 10^{-5}$ using only five clusters with Weak lensing priors taken into account, at a 95% confidence level. These bounds are consistent with existing limits in the literature and tighter than the constraints obtained with the same method by previous studies.

I. INTRODUCTION

Most cosmological observations [1,2] can be explained, to a high degree of precision, within the framework of general relativity (GR). In particular, adding a phenomenological cosmological constant (Λ) [3,4] to the Einstein field equations can account for the late-time acceleration of the Universe [5]. Despite its success in reproducing a wide range of datasets (e.g., [6]), the concordance Λ cold dark matter (ΛCDM) model is not still able to provide a physically acceptable motivation for the nature of the cosmological constant. For this reason, in the last decades, alternative viewpoints have been proposed by allowing additional degrees of freedom that could elucidate the dark energy as a dynamic field (for instance quintessence [7]), or modify GR [8–11] so that it can account for the dark energy effects [8].

One of the most popular wide class of modified gravity (MG) models is represented by the framework of scalar-tensor theories [12–15], where a scalar degree of freedom is added to the gravitational field. The presence of such a scalar field provides an additional contribution to the gravitational force [16,17], leaving (in principle) detectable imprints on the formation and evolution of cosmic structures [18–21]. This new interaction should be suppressed at small scales and high-density regions in order to match the tight constraints of GR. Depending on the implementation of this screening mechanism, the effect of the new (fifth) force on matter density perturbations can be significantly different.

A particularly interesting subset of scalar-tensor models is the chameleon field theory [22–24], where the additional scalar field couples nonminimally to the matter and introduces a fifth force [25]. The screening is achieved by working on the potential associated with the field, making the effective mass very large in high-density regions such that the force is suppressed. The modification of the gravitational interaction becomes important at a large distance from the center of a matter distribution [25,26]. When the fifth force is active, it affects the motion of nonrelativistic objects such as galaxies and hot diffuse gas in galaxy clusters. In particular, the presence of the chameleon field changes the relation between pressure and gravitational potential of the hot intracluster medium (ICM) of a cluster [27–30].

Two main parameters construct the chameleon field model in a galaxy cluster: the first one is β, which is the coupling constant between the chameleon field and matter density, and the latter, ϕ_∞, which is the intensity of the field

*[*]yboumech@sissa.it
[†]sandeep.haridasu@sissa.it
[‡]pizzuti@fzu.cz
[§]mbutt@sissa.it
[‖]bacci@sissa.it
[¶]lapi@sissa.it

044007-1

at a larger distance away from the cluster. Under reasonable assumptions (e.g., [27]) these two parameters describe the modification of gravity completely. Also, the case of $\beta = \sqrt{1/6}$ within the chameleon field scenario describes an $f(R)$ theory [31,32].

We consider that the total mass distribution of a galaxy cluster can be parametrized by a Navarro-Frenk-White (NFW) density model [33–38]; under the assumption of hydrostatic equilibrium, the total gravitational potential of the cluster will affect the pressure of the hot gas [27]. In this paper, we implement the formalism presented in [27,39] to the XMM-Newton Cluster Outskirts Project X-COP data products [40–43], which consists of 12 clusters with well-observed x-ray emission and high signal to noise ratio in the Planck Sunyaev-Zel'dovich (SZ) survey [44], essentially providing both ICM temperature and pressure data over the large radial range of $0.2 \text{ Mpc} \leq r \leq 2 \text{ Mpc}$. While in the current analysis, we probe individual galaxy clusters through hydrostatic equilibrium, a robust and complementary approach relies on the analysis of cosmological simulations [45–48] to assess average or distribution statistics as a function of cosmic time. For instance, the authors in [45] study scaling relations in chameleon type $f(R)$ models from simulations of galaxy clusters, and [49] study variations to the halo mass function.

The paper is organized as follows: in Sec. II we construct our model for the chameleon field and show the solution of this field as applied to galaxy cluster with the assumption of the NFW profile, and at the end of the section we discuss the effect of the modification induced by the presence of the chameleon field on the hydrostatic pressure. In Sec. III we present briefly the X-COP data and then construct the likelihood that we will use with the Monte Carlo Markov chain (MCMC) analysis to generate the chains that constrain our parameter space. In Sec. IV we present our results and discuss them in detail while comparing our constraints with the ones obtained by other galaxy clusters' analyses (e.g., [27,50]). Finally, we further derive our main conclusions in Sec. V.

II. MODELING

In this section, we briefly review the framework of the chameleon screening mechanism, highlighting the main features relevant to our analysis.

A. Screening mechanism

The Lagrangian of the theory includes the usual Einstein-Hilbert Lagrangian plus the scalar field, in addition to the Standard Model fields coupled minimally to gravity [25,51–54],

$$L = \frac{M_{\text{Pl}}^2}{2}R + L_m(\tilde{g}_{\mu\nu}, \psi) + L_\phi, \tag{1}$$

where $L_\phi = -\frac{1}{2}(\partial\phi)^2 - V(\phi)$ and $M_{\text{Pl}} = \frac{1}{\sqrt{8\pi G}}$; the Standard Model fields are represented by ψ and $\tilde{g}_{\mu\nu} = A^2(\phi)g_{\mu\nu}$. In the quasistatic approximation, the equation of motion for the field ϕ can be written as [55]

$$\nabla^2\phi = V'(\phi) - \frac{A'(\phi)}{A(\phi)}T. \tag{2}$$

Here the $'$ represents the derivative with respect to ϕ and T is the trace of the stress-energy tensor of the Standard Model field ψ. One can notice that the chameleon field dynamics is sourced by the trace of the stress-energy tensor as is shown in Eq. (2); the field values depend on the matter component and thus the field behaves in different ways for different matter distributions. We denote $\frac{A'(\phi)}{A(\phi)} = \frac{\beta}{M_{\text{Pl}}}$, which is going to be a constant in the current formalism, and here β is the coupling factor between the field ϕ and the stress-energy tensor T. Finally, we consider only pressureless nonrelativistic matter fields, which implies $T = -\rho_m$.

Therefore we can write

$$\nabla^2\phi = V'_{\text{eff}}(\phi), \tag{3}$$

where

$$V_{\text{eff}}(\phi) = V(\phi) + \frac{\beta\phi}{M_{\text{Pl}}}\rho_m. \tag{4}$$

The form of the potential $V(\phi)$ should guarantee that the gravitational effect induced by this field will be suppressed when we have large matter densities, i.e., the field ϕ is screened and GR is recovered. On the other hand, at lower densities, we want the effect of the field to become important, which will require us to impose that the potential $V(\phi)$ is a decreasing function of ϕ [25], typically a power-law potential $V(\phi) = \Lambda^{4+n}\phi^{-n}$, where Λ and n are constants.

In the region where ϕ is unscreened, an additional fifth force is induced by the gradient of the chameleon field,

$$F_\phi = -\frac{\beta}{M_{\text{Pl}}}\nabla\phi, \tag{5}$$

providing an additional contribution to the Newtonian potential while retaining hydrostatic equilibrium assumption in chameleon gravity.

B. Chameleon field in the cluster of galaxies

In the following analysis, we assume that the total matter density distribution within the galaxy cluster can be modeled as an NFW profile [33],

$$\rho(r) = \frac{\rho_s}{r/r_s(1 + r/r_s)^2}, \tag{6}$$

where ρ_s and r_s are characteristic density and scale radius, respectively. The NFW model has been shown to provide a good description for simulated DM halos (see, e.g., [56]) and for real clusters' data in ΛCDM (e.g., [57,58]), while some other works have further suggested that the NFW profile performs well also in modified gravity scenarios, including chameleon gravity [59–62].

We are interested in finding the solution for the chameleon Eq. (3) in the presence of a matter density distribution given by Eq. (6); in order to do that, we employ the semianalytical approach followed by, e.g., [27]. The idea is that, below some radius r_c, the value of the scalar field in the interior minimizes the effective potential $V_{\text{eff}}(\phi)$, which represents the regime where the chameleon force does not contribute and the solution is obtained by setting $\nabla\phi = 0$ on the left side of Eq. (3). On the other hand, at larger distances, the potential $V(\phi)$ is negligible and the second term in (4) dominates the effective potential. The solution in this regime is obtained by solving $\nabla^2\phi = \beta\phi\rho_m/M_{\text{Pl}}$. Therefore, we obtain the complete semianalytical solution as

$$\phi(r) = \begin{cases} \phi_s[r/r_s(1+r/r_s)^2] = \phi_{\text{int}} \simeq 0 & r < r_c \\ -\frac{\beta\rho_s r_s^2}{M_{\text{Pl}}}\frac{\ln(1+r/r_s)}{r/r_s} - \frac{C}{r/r_s} + \phi_\infty = \phi_{\text{out}} & r > r_c \end{cases}. \quad (7)$$

In the above equation, ϕ_s is a constant that depends on the characteristic density and the parameters of the potential $V(\phi)$. The integration constant C and the radius r_c can be specified by imposing the continuity of the solution and its first derivative at $r = r_c$. Thus we have [27]

$$1 + \frac{r_c}{r_s} \simeq \frac{\beta\rho_s r_s^2}{M_{\text{Pl}}\phi_\infty}, \quad (8)$$

$$C \simeq -\frac{\beta\rho_s r_s^2}{M_{\text{Pl}}}\ln(1+r/r_s) + \phi_\infty r/r_c. \quad (9)$$

The screening radius r_c represents the transition below which the chameleon field is screened, and as shown in Eq. (8), it is completely determined by the other parameters of the model. In particular, the screening radius is strongly dependent on the mass of the cluster $M_{500} \propto r_s^3\rho_s$ [see (20) and (21)]. This implies that in massive clusters the screening mechanism tends to be very efficient, while the fifth force is more active in lower mass halos (e.g., [63]).

Note that the current formalism assumes coupling of the chameleon field to both the dark matter and baryonic mass components and that the total mass of the cluster is modeled using a single NFW mass profile. This formalism is equivalent to that followed in the earlier works [27,50] and is an approximation that the contribution of the baryonic component to the total mass is negligible in the radial ranges explored and that a simple NFW profile is sufficient to model the total mass accurately. Although there is a clear

possibility to introduce varied coupling for the different mass components and the field, this is beyond the scope of the current work. However, it is straightforward to model the gas mass, which accounts for the largest contribution to the baryonic mass, that does not couple with the chameleon field, while the dark component does (see for example [64]) and perform the analysis, which we implement discuss in Appendix A 2.

So far we have described the chameleon formalism within the galaxy cluster sourced only by the self-screening. However, it is important to point out that, the intercluster environmental density distribution can generate an additional contribution to the fifth force [49,65]. This in turn is the interplay between the external and the internal densities distinguished by a scale. For example, [65] employs a scale of $r_{\text{in/out}} = 8$ h^{-1} Mpc (see also [66]) and averages over the environmental effects. Taking into account the strong local constraints, for example, (e.g., $|f_{R0}| \sim 5 \times 10^{-7}$ [67]), the mass ranges ($\geq 10^{14}M_\odot$) of the local ($z \leq 0.1$) galaxy clusters utilized in this work, we infer the environmental effects to be relatively small, providing only a mild weakening of our constraints.

C. $f(R)$ analogy with chameleon field

$f(R)$ gravity [68] is one of the most investigated alternatives of GR at the cosmological level; in this class of models, the Einstein-Hilbert action is modified by adding a generic function of the Ricci scalar:

$$S = \int d^4x\sqrt{-g}\frac{1}{16\pi G}[R + f(R)] + S_m[\psi_i, g_{\mu\nu}]. \quad (10)$$

The functional form of $f(R)$ can be chosen in such a way that the background ΛCDM expansion history is reproduced as close as desired (see, e.g., [69]). The derivative of the function $f_R = \partial f_R/\partial R$ plays a role of a dynamical scalar field which, under certain conditions can be conformally recast into a scalar-tensor model exhibiting chameleon screening (see, e.g., [70]). This is possible in particular if the scalar field $f_R = \partial f_R/\partial R$, called the "scalaron," has a large positive effective mass at high curvature [71].

The field equation for f_R is [69]

$$\Box f_R = \frac{\partial V_{\text{eff}}(f_R)}{\partial f_R}, \quad (11)$$

which is analogous to Eq. (3) with the replacement

$$f_R = \exp\left(-\frac{2\beta\phi}{M_{\text{Pl}}}\right), \quad (12)$$

and $\beta = \sqrt{1/6}$ [27,72]. The value of the scalar field for the background today $f_{R0} = \bar{f}_R(z = 0)$ is proportional to

the present value of the chameleon field at infinity as

$$f_{R0} = -\sqrt{\frac{2}{3}} \frac{\phi_\infty}{M_{Pl}}.$$

In the last decades, several works have placed constraints on $f(R)$ gravity using different probes, both at astrophysical (e.g., [62,67,73,74]) and at cosmological (e.g., [27,49,50,75–79]) scales. Currently, the most stringent bounds on the scalaron are of the order of $f_{R0} \lesssim 10^{-8}$, for the Hu and Sawicki functional form of $f(R)$ ([69]), from galaxy morphology [80], while cosmological analyses limit the background field to be $f_{R0} \lesssim 10^{-6}$ (e.g., [81]).

D. Hydrostatic equilibrium

For a spherical system that contains gas with pressure P and density ρ_g, the hydrostatic equilibrium equation is given by

$$\frac{1}{\rho_g} \frac{dP(r)}{dr} = -\frac{GM(<r)}{r^2}, \tag{13}$$

where $M(r)$ is the mass enclosed within the radius r, and the above equation represents the balance between the force induced by the gas pressure and the gravitational force. However, in the current MG scenario, we have an additional force given by Eq. (5) induced by the existence of the chameleon field, which contributes as a new term in the hydrostatic equilibrium equation as [27]

$$\frac{1}{\rho_g} \frac{dP(r)}{dr} = -\frac{GM(r)}{r^2} - \frac{\beta}{M_{Pl}} \frac{d\phi(r)}{dr}, \tag{14}$$

which upon integration provides

$$P(r) = P_0 - \mu m_p \int_0^r n_e(r) \left[\frac{GM(r)}{r^2} + \frac{\beta}{M_{Pl}} \frac{d\phi(r)}{dr} \right] dr, \tag{15}$$

Where μ is the mean molecular weight, P_0 is an integration constant, i.e., pressure at $r = 0$, and $n_e(r)$ is the electron density at radius r. We further assume the electron density to follow the Vikhlinin profile [82,83],

$$n_e(r) = n_0 \frac{\left(\frac{r}{r_1}\right)^{-\alpha_v/2} \left[1 + \left(\frac{r}{r_2}\right)^{\gamma_v}\right]^{-\epsilon_v/2\gamma_v}}{\left[1 + \left(\frac{r}{r_1}\right)^2\right]^{3\beta_v/2 - \alpha_v/4}}, \tag{16}$$

where we fix $\gamma_v = 3$ as suggested in [82]. The electron density profile above thus contains six parameters. While the original Vikhlinin profile contains nine parameters, we have earlier validated that the six-parameter reduced form is sufficient for the dataset utilized here [84].

III. DATA AND LIKELIHOOD

A. X-COP clusters

We utilize nine X-COP clusters [41], following the formalism utilized in an earlier work [84,85]. We keep the current section brief as the utility of the datasets is equivalent to the aforementioned application. While a total of 12 clusters are available in the X-COP compilation, in the current work we utilize only nine of them excluding A644, A2255, and A2319. The three excluded clusters do not favor the NFW mass profile, which is an integral assumption in obtaining the semianalytical expressions for the field in the formalism adopted here. We however include A1644, which is reported to perform equivalently for NFW and the best-fit Hernquist mass profile. We defer the study of the effects of mass profile assumptions on the constraints on the screening mechanisms to a later communication. We show the final datasets of the electron density (top), and pressure obtained using both x-ray and SZ methods [86] (bottom) in Fig. 1.

B. Likelihood

The complete formalism introduced in Sec. II is described by 10 parameters; two defining the chameleon field (β and ϕ_∞), two for the NFW profile (ρ_s and r_s), the remaining six parameters are from the expression of the electron density given by Eq. (16). The individual likelihood ($-2 \ln \mathcal{L}$) for the pressure and electron density data are then written as
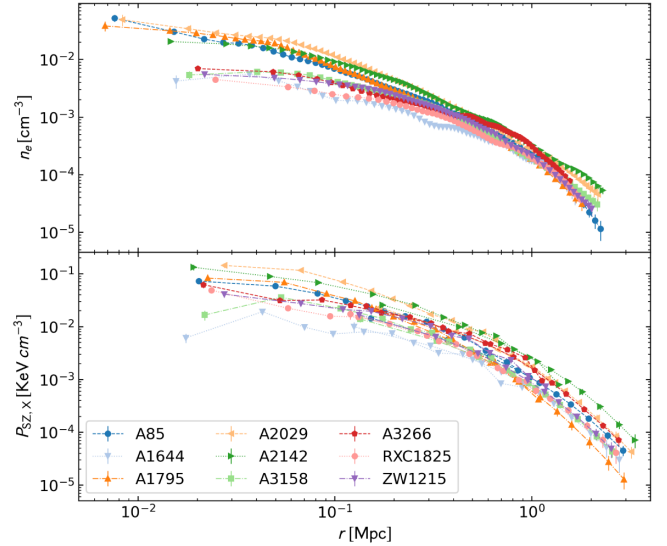
FIG. 1. Top: radial profiles of the electron density [43]. Bottom: pressure data obtained using the Compton effect (P_{SZ}) and the x-ray observations (P_X) [41]. We show the data for all the nine clusters we have utilized in the current analysis.

$$\chi_P^2 = (\mathbf{P}_{SZ}^{obs} - \mathbf{P}_{SZ})\Sigma_P^{-1}(\mathbf{P}_{SZ}^{obs} - \mathbf{P}_{SZ})^T + \ln|\Sigma_p|$$
$$+ \sum_i \left[\frac{(P_X(r_i) - P_{X,i}^{obs})^2}{\sigma_{P_{X,i}}^2 + \sigma_{int}^2} + \ln(\sigma_{P_{X,i}}^2 + \sigma_{int}^2) \right], \qquad (17)$$

$$\chi_{n_e}^2 = \sum_i \frac{(n_e(r_i) - n_{e,i}^{obs})^2}{\sigma_{n_{e,i}}^2}, \qquad (18)$$

respectively. The total χ^2 function is then the summation of individual contributions, upon which we perform the Bayesian analysis and is given by

$$-2\ln\mathcal{L}^{tot} \equiv \chi^2(\Theta_{n_e}, \Theta_{NFW}, \Theta_{MG}) = \chi_P^2 + \chi_{n_e}^2, \qquad (19)$$

wherein $\Theta_{n_e} = \{n_0, r_1, r_2, \alpha_v, \beta_v, \epsilon_v\}$, $\Theta_{NFW} = \{M_{500}, c_{500}\}$, and $\Theta_{MG} = \{\phi_{\infty,2}, \beta_2\}$. Refer to [84,85], for further details on the likelihood and the inclusion of the intrinsic scatter (σ_{int}) parameter.

Therefore, we perform an MCMC analysis over a 10-dimensional parameter space $(n_0, r_1, r_2, \alpha, \beta, M_{500}, c_{500}, \phi_{\infty,2}, \beta_2)$, where the two parameters β_2 and $\phi_{\infty,2}$ are compactified functions of β and ϕ_∞, respectively, and are given by $\beta_2 = \beta/(1+\beta)$ and $\phi_{\infty,2} = 1 - \exp(-\phi_\infty/10^{-4}M_{Pl})$. These new scaled parameters run in the interval [0, 1], making the interpretation of the results straightforward. It is also convenient to use M_{500} and R_{500} instead of ρ_s and r_s, which are related through the following relations [27]:

$$r_s = \frac{1}{c_{500}} \left[\frac{M_{500}}{(4\pi/3)\Delta_c\rho_c} \right]^{1/3}, \qquad (20)$$

$$\rho_s = \frac{M_{500}}{4\pi r_s^3} \left(\ln(1 + c_{500}) - \frac{c_{500}}{c_{500} + 1} \right)^{-1}, \qquad (21)$$

where $c_{500} = R_{500}/r_s$ is the concentration parameter, and we have also $M(r < R_{500}) = M_{500} = \frac{4\pi}{3}R_{500}^3\Delta_c\rho_c$, where $\Delta_c = 500$ and ρ_c is the critical density at the cluster redshift.

We emphasize that in our analysis we implement two different priors on the mass parameter M_{500}; however we also perform the analysis without any restriction on the mass, unlike previous work on other clusters (e.g., Coma cluster in [27]), and therefore we anticipate testing possible degenerate scenarios in the posterior parameter space (allowed at some range of the virial mass), this is discussed at length in Appendix A 1.

C. Weak lensing mass priors

Chameleon gravity belongs to a subset of scalar-tensor theories for which the gravitational potential inferred by lensing techniques corresponds to the Newtonian potential (i.e., the contribution of the fifth force does not affect null geodesics). As such, we can implement the information

TABLE I.   We show the weak lensing masses utilized as mass priors for the five clusters available from [87].[a]

Cluster	$M_{500}[10^{14}M_\odot]$
A85	5.7 ± 2.2
A1795	9.3 ± 2.2
A2029	12.1 ± 2.5
A2142	9.7 ± 2.3
ZW1215	3.5 ± 2.2

[a]We utilize the mass estimated using the NFW mass profile for consistency, please see the Table A2 in [87]. See also Appendix A 1 for more comments.

provided by lensing estimation as prior on the "true" cluster mass M_{500}, as done in, e.g., [27,50]. We utilize the estimates of M_{500} obtained using weak lensing analyses in [87], wherein no information on the shape (c_{500}) of the mass profile is available. However, we find that mass information is available only for five clusters in the sample, A85, A1795, A2029, A2142, and ZW1215. In Table I, we show the mean and 1σ uncertainties on M_{500} for these clusters, taken from [87]. We beforehand anticipate that the constraints on mass parameters we shall obtain using the X-COP data will be much tighter than the uncertainty of the weak lensing masses we use as priors.

We perform a full Bayesian analysis utilizing Eqs. (17) and (18) to define the likelihood, through the publicly available EMCEE[1] package [88,89], which implements an affine-invariant ensemble sampler. To analyze the MCMC chains we utilize either the CORNER and/or GetDist[2] [90] packages. Also, we impose uniform flat priors on all the parameters, specifically for the modified gravity parameters $\{\beta_2, \phi_{\infty,2}\} \in [0.001, 1.0]$. As the current analysis provides posteriors of exclusion within the parameter space, always including the GR scenario, to the first order we refrain from performing any model selection, which is bound to select GR with higher preference.

Finally, we implement a simple importance sampling-like routine to combine the constraints in the Θ_{MG} parameter space, obtained using the individual clusters. Given that the parameters Θ_{NFW} and Θ_{n_e} are cluster specific and are not expected to affect the joint constraints on the Θ_{MG} parameters which are of a global theory. Therefore, we combine the MCMC samples of the Θ_{MG} parameters obtained from each of the clusters where the sample density represents the values of the posterior (Bayesian confidence levels). We take a subsample of thinned MCMC samples of equal size and resample the joint posteriors. Essentially, this approach is equivalent to marginalizing all the cluster-specific parameters, while not being able to see the effect of the joint analysis on them. The results of the combined analysis are given in Sec. IV C.

_____

[1]http://dfm.io/emcee/current/.
[2]https://getdist.readthedocs.io/.

IV. RESULTS

We begin by presenting the constraints on the $\{\phi_{\infty,2}, \beta_2\}$ parameter space for each of the nine clusters as shown in Fig. 2, utilizing the internal mass prior, elaborated in the next paragraph. The blue and light blue regions depict the allowed parameter space at 2σ and 3σ, respectively, while the white region consequently is excluded by the current data at 3σ confidence level. We can already notice for all clusters that, at low β_2 (equally β), $\phi_{\infty,2}$ is unconstrained: as

the coupling constant becomes negligible, the chameleon field is decoupled from matter and can no longer be constrained. Meanwhile, at large values of β, that is when $\beta_2 \simeq 1$, the coupling is too strong that the entirety of the clusters will be screened, i.e., the screening radius is larger than the size of the cluster in which case also all values of $\phi_{\infty,2}$ are allowed. We also find that at low values of β_2, a slightly larger part of the parameter space is excluded compared to the results presented in [27,50], which in our
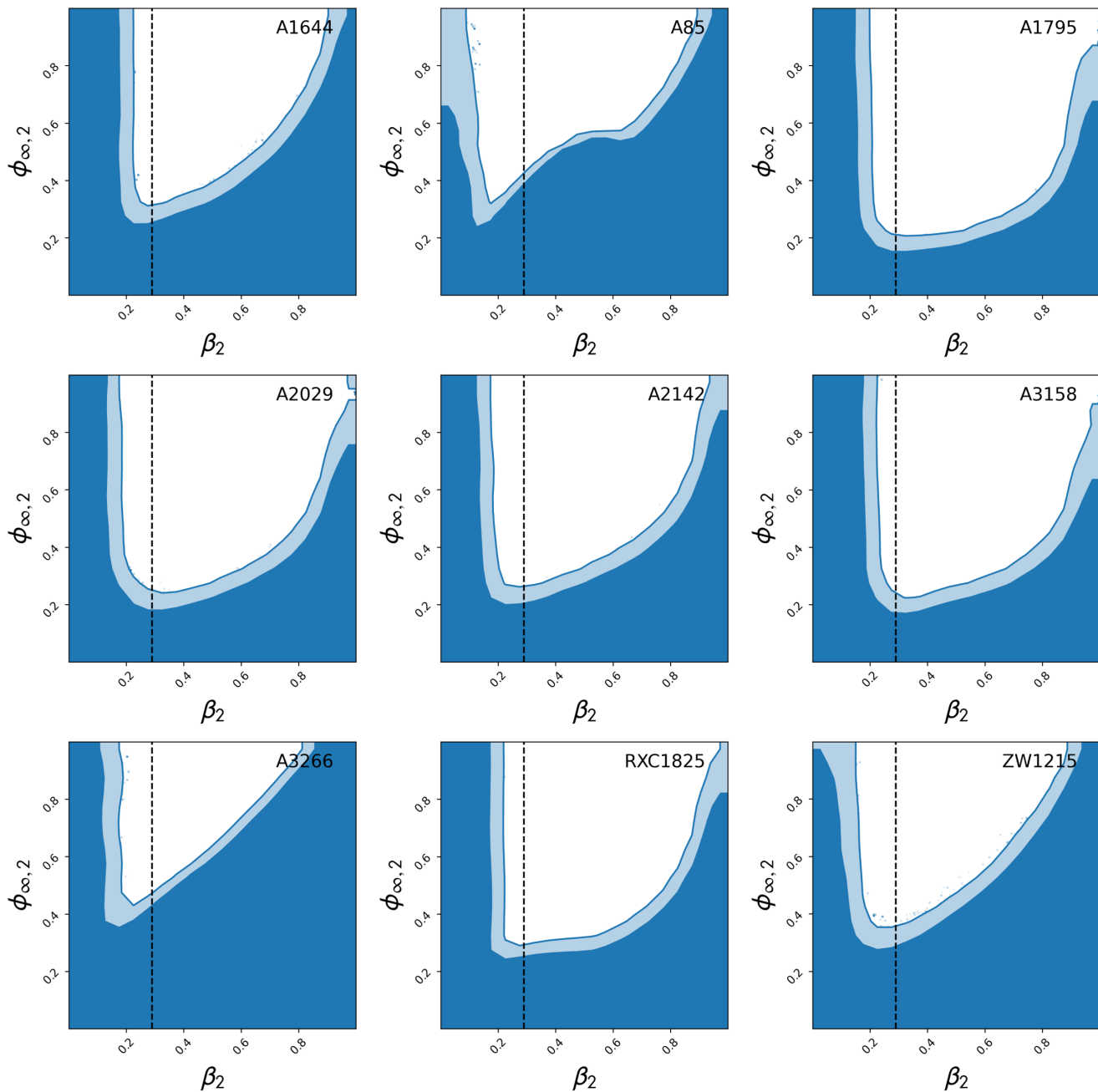
FIG. 2. 95%, 99% C.L. contours for all the clusters utilizing the internal mass prior. The vertical line shows the $\beta_2 \sim 0.29$, corresponding to the $f(R)$ scenario where $\beta = \sqrt{1/6}$.

results extends to $\beta_2 \sim 0.2$. In Fig. 2, this lower limit is what we see as an almost vertical line in the contours that separates the blue allowed region from the white excluded one for lower values of β_2. On the other hand, compared to the same previous results, we find that the lowest possible values for $\phi_{\infty,2}$ are also lower, which further reduces the allowed region providing tighter constraints in our analysis. This is mainly due to the effect of the internal mass prior, as we will discuss below.

We also point out that in the plots an exponential-shaped bound appears in all of the posteriors of $(\phi_{\infty,2}, \beta)$, which is due to the fact that the formalism inherently takes into account the assumption that the critical radius r_c is a positive quantity. From Eq. (8) it can be shown that this is equivalent to regions below the curve of the following equation:

$$\phi_{\infty,2} = 1 - \exp\left(-\frac{\beta_2}{1-\beta_2}\frac{\rho_s r_s^2}{10^{-4} M_{\rm Pl}^2}\right). \qquad (22)$$

As mentioned before, the contours of Fig. 2 are obtained by adding a prior on the parameter M_{500}. This is because utilizing only the hydrostatic equilibrium data leads to a strong degeneracy in the $\{M_{500}, \beta_2\}$ parameter space, which prevents us from placing any stringent bounds in most of the cases. In earlier analyses this degeneracy was broken by aiding the hydrostatic data with the mass priors obtained from weak lensing analyses. We further elaborate on this in Appendix A 1 (cf., Fig. 6).

To assess the constraints while excluding this degeneracy we eliminate the lower mass regions by considering a lower limit of $\beta_2 > 0.5$ and constrain the posteriors for the $\{M_{500}, c_{500}\}$, following which we construct the mass and concentration priors, also taking into account the corresponding covariance and reperform the analysis by expanding the range of $\beta_2 \in (0.0, 1.0)$, as shown in Fig. 2. Hereon we denote this prior as internal mass prior and elaborate in Sec. IV B. We find that this degeneracy is usually present within $\beta_2 < 0.5$, corresponding to $\beta < 1$, accounting for a decrease in the values of M_{500} while the values of β increase, following the expression of the thermal pressure in Eq. (15). In clusters A85 and RXC1825 however, we find this degeneracy to extend beyond $\beta > 1$. In particular, for A85, we see that the internal mass prior is completely unable to even reduce the degenerate region.

We then show the quantitative results of our analysis in Table II we show the results of our analysis for the nine X-COP clusters used in this work. We present in the first column the 68% C.L. of the concentration parameter c_{500} and the mass M_{500} with the internal mass prior elaborated above. We also present the 95% C.L. limits on the value of the field $\phi_{\infty,2}$ for $\beta = \sqrt{1/6}$, which corresponds to the $f(R)$ subclass of chameleon model, presented in Sec. II. In the subsequent columns we present the values at 95% C.L. we obtain for the field $\phi_{\infty,2}$ when imposing the weak lensing mass prior presented in Fig. 3 and no mass prior, respectively, which we added for completeness. Within parentheses we show the conversion of $\phi_{\infty,2}$ into $|f_{R0}|$ to get explicit constraints on $f(R)$ models. As can be seen, comparing the internal mass prior and no prior scenario, the constraints deteriorate substantially for all the clusters except A85 and A3158. In the case of A85, these posteriors are dominated by the presence of the degeneracy in $\{M_{500}, \beta_2\}$ parameter space. On the other hand, cluster A3158 shows the least observed degeneracy. As for mass profile constraints, c_{500} and M_{500}, presented in the first two columns of Table II, are

TABLE II. Constraints on parameters $\{c_{500}, M_{500}\}$ and $\phi_{\infty,2}$ at 68% and 95% C.L., respectively, from the analysis of each cluster in the sample. The limits are obtained with three different methods: from columns two to four, the inclusion of an internal mass prior to avoid the statistical degeneracy between mass and MG parameters, as discussed in Appendix A 1. Column five: Weak lensing (WL) mass prior—which is available only for five clusters. Column six: no mass prior is taken into account. Note that the bounds on M_{500} and c_{500} are shown only for the first case. The constraints on $\phi_{\infty,2}$ are all presented for $\beta = \sqrt{1/6}$, which corresponds to $f(R)$ gravity. The corresponding bounds on the parameter $|f_{R0}|$ are shown inside the parentheses.

Cluster	Internal mass prior			WL mass prior	No mass prior
	c_{500}	M_{500} $[10^{14}M_\odot]$		$\phi_{\infty,2}(|f_{R0}|[10^{-5}])$	
A85	$2.05^{+0.07}_{-0.07}$	$6.13^{+0.18}_{-0.18}$	0.272(2.592)	0.279(2.671)	0.276(2.637)
A1644	$1.13^{+0.11}_{-0.14}$	$2.95^{+0.20}_{-0.20}$	0.226(2.092)	/	0.942(23.25)
A1795	$3.17^{+0.14}_{-0.14}$	$4.48^{+0.15}_{-0.15}$	0.146(1.289)	0.319(3.137)	0.874(16.91)
A2029	$3.20^{+0.13}_{-0.13}$	$7.70^{+0.24}_{-0.24}$	0.208(1.904)	0.396(4.117)	0.942(23.25)
A2142	$2.22^{+0.08}_{-0.08}$	$8.32^{+0.19}_{-0.19}$	0.198(1.802)	0.213(1.956)	0.498(5.627)
A3158	$1.98^{+0.14}_{-0.14}$	$3.96^{+0.16}_{-0.16}$	0.216(1.987)	/	0.281(2.694)
A3266	$1.61^{+0.11}_{-0.11}$	$7.21^{+0.28}_{-0.32}$	0.245(2.295)	/	0.804(13.30)
RXC1825	$2.54^{+0.20}_{-0.24}$	$3.90^{+0.17}_{-0.15}$	0.146(1.289)	/	0.358(3.619)
ZW1215	$1.40^{+0.09}_{-0.09}$	$7.43^{+0.29}_{-0.29}$	0.342(3.417)	0.892(18.17)	0.567(6.834)
Joint	$\cdots$	$\cdots$	0.106 (0.915)	0.130 (1.139)	$\cdots$
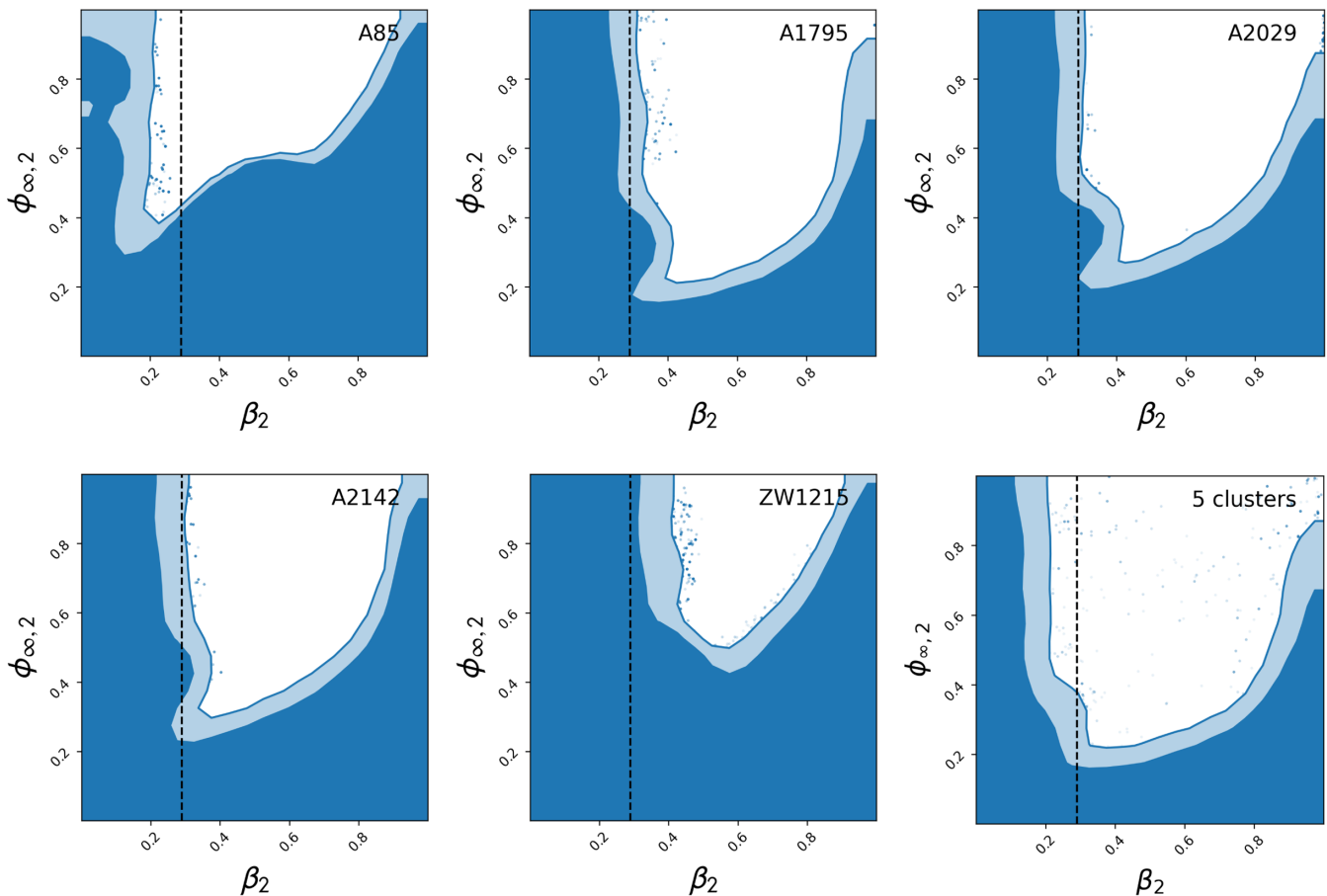
FIG. 3.   95% and 99% C.L. contours for weak lensing priors for five of the clusters. In the lower right panel, we present the joint constraint obtained by combining all five clusters. The dashed vertical line represents the $\beta = \sqrt{1/6}$, corresponding to the $f(R)$ scenario.

the same as the GR values up to a 1σ confidence level [84], they are very much in agreement with those estimated for DHOST gravity as presented therein.

One can also notice that in the case where we consider an internal mass prior the constraints get considerably tighter, for instance, the A1795 field value is eight times tighter than the one with no mass prior and three times than the one with the weak lensing prior (which is yet a good constraint compared to the one with no mass prior). Also, we point out that the two-dimensional posteriors are visually much tighter than those previously presented for Coma cluster [27] and XMM clusters in [50]. We later perform a more qualitative comparison for the $|f_{R0}|$, in the $f(R)$ scenario.

A. Constraints using weak lensing mass prior

In this section, we present the constraints obtained on the five clusters for which the weak lensing mass priors are included from the results of [87], namely A1795, A2029, A2142, A85, and ZW1215. While aiding in the analysis as an independent prior on the mass of the cluster, this also reduces the aforementioned degeneracy between the

$\{\beta_2, M_{500}\}$ parameters. The constraints on the modified gravity parameters are shown in Fig. 3. Note that for the cluster ZW1215 alone the inclusion of the WL prior does not aid the constraint and on the other hand, slightly deteriorates the upper limits. This is clearly the case, as the prior itself is an estimated lower value aiding the degeneracy region, with a mass of order $3.5[10^{14}M_\odot]$.[3] However, this does not hinder our ability to constrain the modified gravity parameters in the joint analysis, as discussed in Sec. IV C. And it is apparent that the degeneracy that remains in the A85 cluster does not affect the joint constraint being guided by the other cluster.

As expected, we notice that the WL mass prior is capable of reducing the degeneracy elaborated earlier and making the posteriors in the $\{\phi_{\infty,2}, \beta_2\}$ slightly more constrained. Note however that the WL mass estimates do present a mass bias (b $= M_{500}^{\mathrm{WL}}/M_{500}^{\mathrm{HS}}$), which is slightly larger than unity ($b \sim 1.18 \pm 0.12$) [41] at R_{500}. However, in terms of

---

[3]Note that [87] also present the weak lensing mass for the ZW1215 cluster, including others using varied methods, which is higher $\sim 7 \times 10^{14}[M_\odot]$.
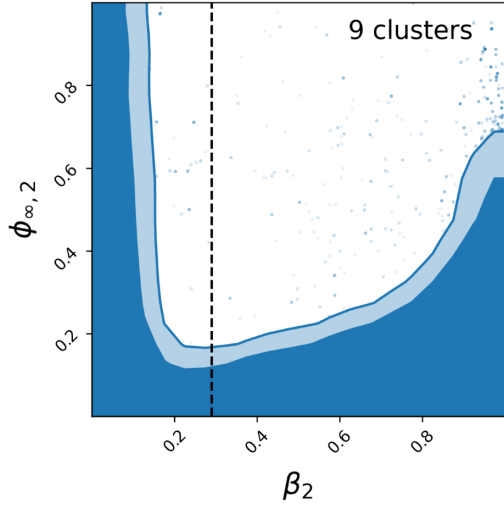
FIG. 4. 95% and 99% C.L. contours for joint constraint utilizing the internal mass priors for nine of the clusters. The dashed vertical line represents the $\beta = \sqrt{1/6}$, corresponding to the $f(R)$ scenario.

the constraints, even the inclusion of the WL mass prior is not able to remove the degeneracy completely, which can be seen as a mild bump in the posteriors presented in Fig. 3. This is clearly due to the larger uncertainties on the WL masses in comparison to the constraints on M_{500} obtained from the hydrostatic equilibrium. Our formalism here validates that having a well-constrained independent mass estimate from the WL method, where the weak lensing potential is unaffected by the chameleon gravity and can be very beneficial for constraining the parameters.

B. Parameter degeneracy

Alongside obtaining the constraints on $\{\phi_{\infty,2}, \beta_2\}$ parameters, we also comment on the degeneracy(s) that we notice between the cluster mass profile parameters and the modified gravity parameters. As can be seen in Fig. 6, an increase in β_2 or $\phi_{\infty,2}$ is compensated by lower values of M_{500}. This is not surprising, given the structure of the modified Newtonian potential in Eq. (15). This degeneracy is also visible in the marginalized posterior distribution of $\phi_{\infty,2}$ and β_2 as a bump, highlighting the necessity of a mass prior to hydrostatic equilibrium data. In fact, we can notice that the degeneracy reduces as soon as we add additional information on M_{500}, and the tighter this mass prior, the lesser the degeneracy we have. Earlier hydrostatic equilibrium analysis which always considered the WL counterpart did not find such a degeneracy, for instance using COMA cluster in [27] and XMM cluster in [50].

We can also see this quantitatively from the condition we impose in our model to estimate the screening radius, which gives a direct relation between M_{500} and β. In particular, replacing Eqs. (20) and (21) into (8) one can write

$$1 + \frac{r_c}{r_s} \sim \frac{1}{M_{500}^{-5/2}} \frac{\beta}{\phi_\infty} f(c_{500}). \quad (23)$$

Here $f(c_{500})$ is a function that only depends on the shape of the profile (c_{500}). At this stage, if we impose the condition that maps all negative r_c to $r_c \sim 0$ we get from above $\frac{\beta}{\phi_\infty} \sim M_{500}^{-5/2}$, this means that when the coupling constant β is low, the mass gets higher, which creates a region where the higher the mass, the lower the coupling and vice versa, as can be seen in Fig. 6. Also within the hydrostatic equilibrium equation, the contribution of the gravitational force and the fifth force, are scaled by M_{500} and β, respectively. The summation of these two forces provides the derivative of the pressure and not knowing the integration constant $P(r = 0)$ beforehand allows only the shape to be constrained and hence the degeneracy between these two forces is propagated to the corresponding parameters.

One can also notice in the $\{\phi_{\infty,2}, M_{500}\}$ plot of Fig. 6 that the same degeneracy holds: lower values of the mass correspond to slightly higher $\phi_{\infty,2}$ (equally ϕ_∞). This region appears only for low mass values and coupling constant $\beta_2 < 0.5$ (i.e., $\beta < 1.0$). As for the higher masses limit, this degeneracy disappears with the coupling strength approaching $\beta_2 \to 0$. Therefore to avoid such a statistical degeneracy we construct an internal mass prior based on the mass values we get for $\beta_2 > 0.5$ and then run the MCMC chain again to get the new posteriors, and this will erase the degeneracy issue as shown in Fig. 2. Alternatively, adding the WL mass prior will remarkably reduce the degeneracy region as shown in Fig. 6 and the posteriors are shown in Fig. 3.

C. Joint analysis

Considering that the clusters utilized in the analysis are independent datasets, we explore the possibility to obtain joint constraints on the modified gravity parameters $\{\phi_{\infty,2}, \beta_2\}$. In principle, the background field should evolve in cosmic time. However, given the small redshift range ($0.04 \leq z \leq 0.09$) spanned by the sample, we can safely neglect any redshift dependence and assume $\phi_\infty(z) \sim \phi_\infty(z = 0)$, essentially constraining the local value of the field. In Fig. 4 and the lower right panel of the Fig. 3, we show the joint constraints using nine clusters and five clusters with the WL mass priors, respectively. First, the overall posterior parameter space in Fig. 4 is greatly reduced when the 9 clusters are combined displaying the ability of the current hydrostatic data to constrain the chameleon screening model, improving the constraints from the earlier analysis in [27,50]. Note that the internal mass prior plays a very important role in allowing such tight constraints. The joint constraints using the five clusters using the WL mass prior as well is a tighter constraint with a mild residual of the degenerate region.

D. Joint constraints on $f(R)$ gravity

In the following we use the results of our joint analysis of the chameleon parameter space to place constraints on the background scalaron field f_{R0}, neglecting the redshift dependence. Starting from the joint posteriors of Figs. 4 and 3, we consider the slice of parameter space $(\beta_2, \phi_{\infty,2})$ for a constant value of $\beta_2 \sim 0.29$ (i.e., $\beta = 1/\sqrt{6}$). We then derive the corresponding posterior $P(\phi_\infty|\beta = 1/\sqrt{6})$, which is further related to f_{R0} as a particular case of the chameleon coupling, discussed at the end of Sec. II. In
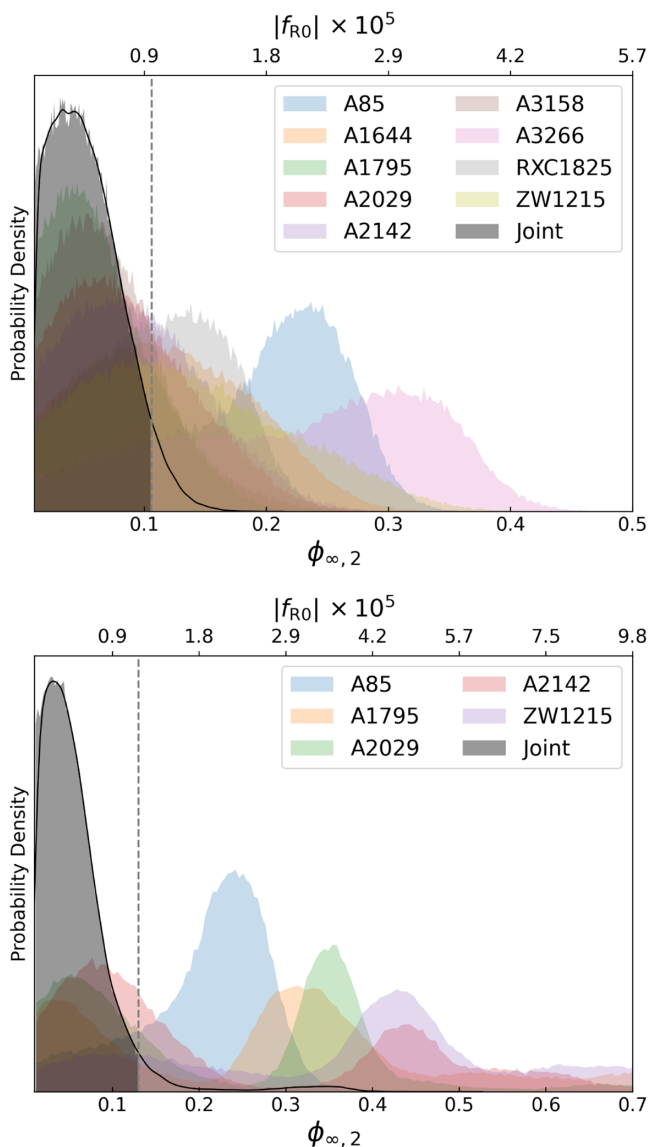
FIG. 5. Probability distributions for $\phi_{\infty,2}$ (f_{R0} depicted on the top axis) obtained for the specific case of $\beta = 1/\sqrt{6}$ for all the clusters within the compilation and the consequent 95% C.L. regions for the joint analysis (shaded in gray). Top: nine clusters with an internal mass prior. Bottom: five clusters for which a WL mass prior was available. Please note the difference in the limits of axes in the two figures.

Fig. 5 we plot the distributions $P(f_{R0})$ for the nine-clusters joint case, assuming internal mass priors (top), and for the combination of five clusters with weak lensing priors on M_{500} (bottom). The colored areas in gray indicate the regions corresponding to the 95% C.L. As already mentioned, the mass priors play a fundamental role in breaking the degeneracy among the model's parameters. In the case of weak lensing information, the priors are not sufficient to remove all the degeneracy, resulting in a bump in the scalaron distribution of individual clusters. Although the individual clusters in the case of WL priors show a bimodal distribution (except for A85), the joint analysis however is capable to providing a tighter constrain owing to the fact that the second mode in the posterior distribution is spread across the values of the $\phi_{\infty,2}$ and consequently in f_{R0}. As our final constraints, we quote

$$|f_{R0}| < 9.1 \times 10^{-6},$$

at 95% C.L. for the nine-clusters combined analysis, and similarly

$$|f_{R0}| < 1.1 \times 10^{-5},$$

for the five-cluster weak lensing case.

Within the posteriors of the $\phi_{\infty,2}$ shown in the bottom panel of the Fig. 5, one could distinguish three distinct contributions (except for A85). The first peak which mainly contributes to joint constraint is marginalized for the M_{500} that does not include the degeneracy, with either of $\{\phi_{\infty,2}, \beta_2\}$. While the second peak is an outcome of slightly lower masses, and larger values of the c_{500} parameter, essentially implying a modification to the shape of the mass profile. Finally, the extended tail of the distribution seen for $\phi_{\infty,2} > 0.5$ is due to the mild degeneracy between $\{\phi_{\infty,2}, M_{500}\}$, for even lower values of M_{500}. However, in the joint analyses, the latter two features do not amplify being varied nonoverlapping distributions.

Earlier in [27], a constraint of $|f_{R0}| < 6 \times 10^{-5}$ was set using the hydrostatic and weak lensing observables of the Coma cluster at $z = 0.02$, which is even more local in comparison of the redshift range $z \in \{0.04, 0.09\}$ of current X-COP clusters. In this context all the individual clusters in the current analysis provide a tighter constraint (see column 4 of Table II) and almost an order tighter joint constraint when combining all the data. Our constraint here is also tighter with respect to to the 58 stacked cluster analysis in [50], which considers XMM cluster survey and CHFTLenS weak lensing observations in a large redshift range of $z \in \{0.1, 1.2\}$. In principle, such a joint analysis considers no cosmological evolution in the field. Other works that used galaxy clusters estimated $|f_{R0}| < 10^{-5}$ (e.g. [76,77]); moreover, [63] forecasted a value of $|f_{R0}| < 10^{-6}$ from the combination of lensing and kinematics mass profile reconstructions of a reasonable sample (~ 10) of

clusters. Our analysis confirms that constraints of the same order of magnitude can be reached with a combination of high-quality x-ray cluster data with physically motivated priors in the cluster masses. It is also worth noticing that the bounds derived here are model independent, i.e., no particular functional form for $f(R)$ has been assumed.

V. CONCLUSIONS

In this paper, we have implemented a formalism, following what done in previous works [27,50], to test the chameleon screening in galaxy cluster utilizing the hydrostatic equilibrium data. We have constrained the two parameters describing the chameleon field, the coupling constant β and the value of the field at infinity ϕ_∞ by analyzing the dynamics of nine galaxy clusters in the X-COP sample. The chameleon field manifests as a fifth force beyond a certain critical screening radius within a cluster that adds up to the gravitational potential. By performing a full Bayesian analysis of the x-ray-emitting gas pressure and the SZ pressure, along with the electron density, we obtain limits on the aforementioned parameters, essentially excluding a part of the parameter space for this modified gravity scenario. We summarize the results as follows:

(1) We find that adding a physically motivated mass prior to our analysis will give a remarkably tight constraint, breaking the degeneracy among model parameters (see also Appendix A 1). For instance, as the main result we present Fig. 2, where we construct an internal mass prior by eliminating the low mass degenerate regions and use the posterior as a prior in the new MCMC chains, obtaining very tight constraints on $\{\beta, \phi_\infty\}$ compared to previous analysis of Coma cluster [27] and stacked analysis of XMM clusters [50].

(2) We have then included additional information on M_{500} from weak lensing analysis in [87] (see Fig. 3). While the results are comparable to what we obtained with the internal mass prior, the weak lensing data are not tight enough to remove the degeneracy completely.

(3) We present our final results in Table II where we show all the constraints obtained using different mass priors and report a joint constraint eventually on the $f(R)$ class of models presented in Sec. II.

(4) We note that marginalizing or fixing the electron density profile shows no effect on the constraints obtained for the chameleon parameters (see Fig. 7). And briefly discuss the change in constraints when gas mass is included in the analysis without being coupled to the chameleon field.

It is worth pointing out that we have considered only clusters for which the total mass profile (in GR) is well described by the NFW model. Although this choice is physically well motivated, it is important to explore the effect of different mass parametrizations that may better

describe the total matter distribution within galaxy clusters in theories of gravity alternative to GR. Indeed the NFW model, despite its wide range of applicability over different scales, might not be the best profile to reproduce the mass distribution of halos in a modified gravity scenario (see, e.g., [91] and references therein). In particular, the efficiency of the screening mechanism in chameleon gravity is strictly dependent on the mass model, as one can see from Eq. (4). Finally, in Appendix A 4 we make a validation of our constraints with the concentration-mass scaling relation present in the literature.

Moreover, as shown in [63], the inclusion of kinematics of the member galaxies in clusters to constrain the chameleon parameters can help in reducing the degeneracy even further: both galaxy and ICM move at nonrelativistic velocities, following the same gravitational potential. However, the underlying physics is different, leading to distinct degeneracy among model parameters. We will investigate these aspects in an upcoming work.

ACKNOWLEDGMENTS

APPENDIX

1. Effects of mass prior

In this section, we briefly comment on the different priors choices and systematics due to the electron density data modeling, considering cluster A2142 as an exemplar. In Fig. 6, we compare the posteriors obtained, with and without the inclusion of the mass priors. The strong degeneracy between the mass of the cluster (M_{500}) and the chameleon parameters, can be clearly noticed in the contours shown in blue, deforming the two-dimensional Gaussian expectation in the M_{500} parameter space. When the WL mass prior is added (shown in red), the degeneracy region shrinks providing more exclusion region in the chameleon parameters. This is completely independent of any analysis choices made and only due to the WL mass prior which is an independent observable, therefore aiding
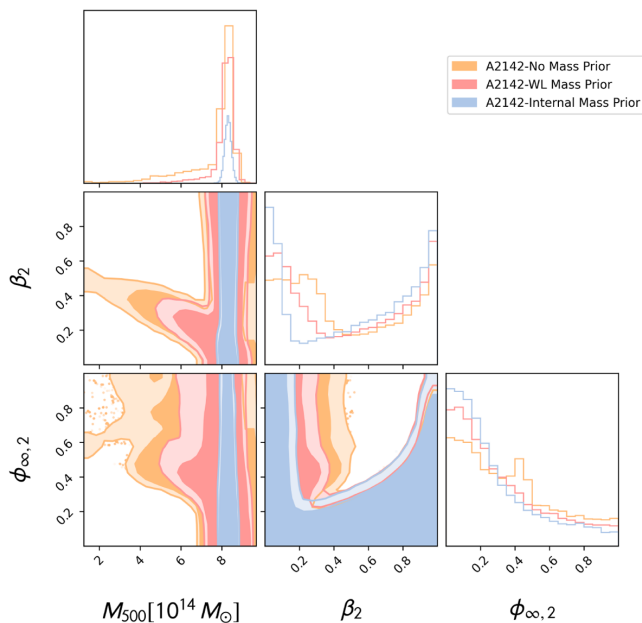
FIG. 6.   We show the 95% and 99% C.L. contours for A2142 cluster, where the orange contours represent the ones with no mass prior is taken into account, the red ones with the weak lensing mass prior and the blue ones correspond to the internal mass prior case. We notice that the degeneracy region gets reduced when we have an additional mass prior.

to the constraints. In blue, we show the posteriors when the internal mass prior is considered. As elaborated in Sec. IV, this prior is taken from the posterior, when the MCMC analysis is performed with a $\beta_2 > 0.5$ limit. And as expected the mass degeneracy is completely eliminated finding much tighter constraints in the exclusion region. Note that both the mass priors do not modify the constraints of the chameleon parameters for $\beta_2 > 0.5$.

2. Effects of gas mass and fixing density (n_e) profiles

In Fig. 7, we show as an example the comparison of the contours showing the constraints when the electron density parameters are allowed to vary in MCMC analysis against the case when they are fixed to the mean values obtained from the former case. We find that the uncertainty in the electron density parameters does not add to the overall uncertainty in the chameleon parameter space. This can be understood straightaway as there is no expected coupling to the gas density and the mass profile of the dark matter is modeled via the NFW profile and is assumed to be equivalent to the total mass of the cluster. Noting this as an advantage, we first perform the analysis marginalizing the electron density parameters and later fixing them to obtain our final results presented in Sec. IV. This essentially helps to span the $\{\phi_{\infty,2}, \beta_2\}$ parameter space effectively in comparison to the case when all the 10 parameters are allowed to vary, where the posteriors might be affected by the sampling methods.
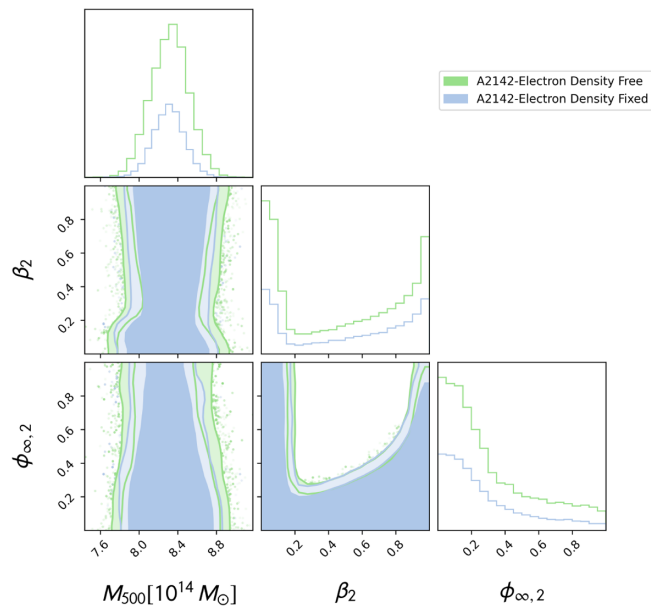
FIG. 7.   We show the 95% and 99% C.L. contours for A2142 cluster, wherein the blue contours represent analysis where electron density parameters are fixed. The green contours show the case where the electron density parameters are marginalized upon.

As discussed earlier in Sec. II, we test for the possibility to model the gas mass and the dark matter components separately assuming that only the dark matter couples with the chameleon field. We show the results of the same in Fig. 8, which can be contrasted against Fig. 6 for the same
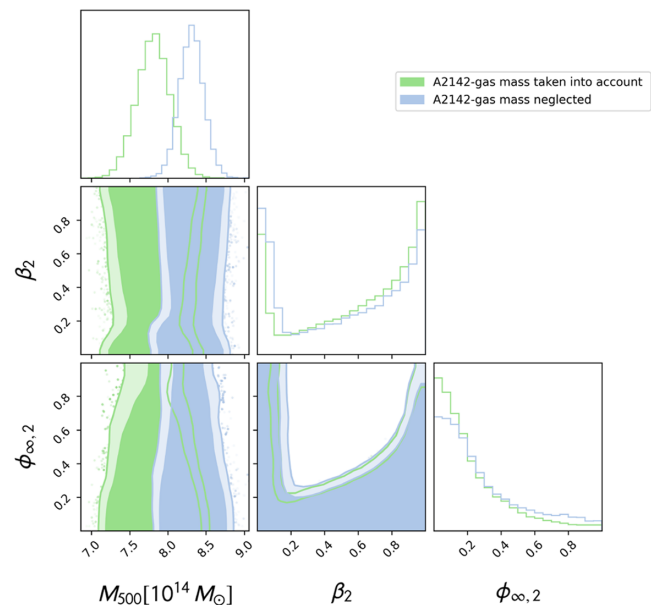
FIG. 8.   We show the 95% and 99% C.L. contours for A2142 cluster, wherein the blue contours represent analysis where the gas mass is neglected. The green contours show the case where the gas mass is taken into account in the total pressure.

cluster assuming one mass profile that models both the gas and dark matter components coupled to the field. We verify that this scenario, which is capable of mildly addressing the degeneracy between the M_{500} and the β_2 parameter, eventually does not affect the final constraints on the chameleon parameters. Also reflecting as a change in the vertical cutoff for the lower values of β_2, which is partially due to the reduction in degeneracy. Also implying that when the coupling between the baryons (gas) and chameleon is not accounted for correctly, considering a single mass profile as a proxy for both dark and baryonic components is a more conservative approach.

3. Alternative weak lensing mass priors

As noted earlier in Secs. III and IV, [87] provide weak lensing mass estimates using both the NFW density profile assumption (M_{500}^{NFW}) and an alternative method, fitting the mean convergence within an aperture radius (M_{500}^{ap}), which is independent of the mass profile assumptions. First, we notice that the two masses presented therein are mostly in agreement, and utilizing either of them does not change our final constraints, except for the cluster ZW1215 with $M_{500}^{ap} \sim 2 \times M_{500}^{NFW}$. We validate that replacing the ZW1215 prior in Table I with the higher M_{500}^{ap}, considerably improves the exclusion region, however, the joint constraint remains unaltered. Therefore, we remain to present our final results with the WL mass priors as the values of M_{500} found assuming the NFW mass profile.

4. $c(M)$ relationships as priors

Since two of the main parameters in our study are c_{500} and M_{500}, we can straight away compare our constraints with the well-established scaling relationships between the concentration c_{200} and the corresponding mass M_{200} in galaxy clusters [94,95]. These relations can be extended to the case of modified gravity namely in the case of Hu-Sawicki $f(R)$ model used above, see [96,97]. As elaborated in [96] the current relation [95] holds also for all but low masses at low redshifts and within the $f(R)$ case considering small values of $|f_{R0}|$. Both these conditions are met for the nine clusters used in our analysis (see Table II). Since we have this well-known relation between the concentration and the mass validated against the independent analyses of
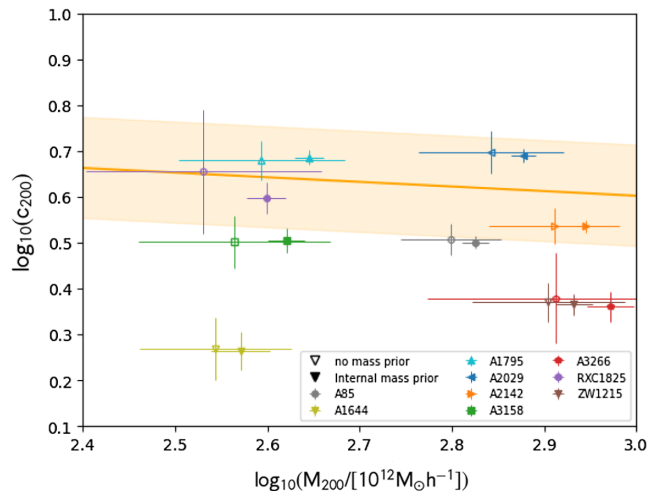
FIG. 9. We plot the $c_{200}(M_{200})$ relation against the nine cluster in our analysis. The solid orange line represents the relation in [94] with a lognormal scatter of 0.11 dex shown as the shaded region.

the clusters, one could utilize it as a prior when assessing the modified gravity parameters, perhaps eliminating some degeneracy in the posteriors. However, note that the dispersion of the scaling relation is larger by an order $\gtrsim 2$ for at least six of the clusters which are well within the 1σ region, and for three other clusters the constraints are in agreement at $\sim 2\sigma$. We show a comparison of our constraints and the scaling relation taken from [94] in Fig. 9. for the case without any mass prior and with the internal mass prior, in open and filled markers, respectively. We see from the plot that the internal mass prior shifts the masses towards higher values and makes the mass tighter (see Sec. IV B), as expected. However, this also validates that adding the scaling relation as a prior would have a mild to no effect on the position of these clusters in the $c(M)$ space. Note, for example, that cluster A1644, which is the most discrepant with respect to the scaling relation, also prefers a mass model other than NFW [41]. Therefore, we defer the analysis utilizing the scaling relation as prior to future work, assessing also the effects of assumed mass models on mass and modified gravity parameters, simultaneously.

[1] R. Adam *et al.* (Planck Collaboration), Astron. Astrophys. **594,** A1 (2016).

[2] P. A. R. Ade *et al.* (Planck Collaboration), Astron. Astrophys. **594,** A13 (2016).

[3] S. Weinberg, Rev. Mod. Phys. **61,** 1 (1989).

[4] P. Bull *et al.*, Phys. Dark Universe **12,** 56 (2016).

[5] B. S. Haridasu, V. V. Luković, R. D'Agostino, and N. Vittorio, Astron. Astrophys. **600,** L1 (2017).

[6] Planck Collaboration, Astron. Astrophys. **641,** A1 (2020).

[7] R. R. Caldwell, R. Dave, and P. J. Steinhardt, Phys. Rev. Lett. **80,** 1582 (1998).

[8] S. Tsujikawa, Lect. Notes Phys. **800,** 99 (2010).

[9] S. Nojiri and S. D. Odintsov, Phys. Rep. **505**, 59 (2011).

[10] T. Clifton, P. G. Ferreira, A. Padilla, and C. Skordis, Phys. Rep. **513**, 1 (2012).

[11] S. Nojiri, S. D. Odintsov, and V. K. Oikonomou, Phys. Rep. **692**, 1 (2017).

[12] D. Langlois and K. Noui, J. Cosmol. Astropart. Phys. 02 (2016) 034.

[13] M. Crisostomi, K. Koyama, and G. Tasinato, J. Cosmol. Astropart. Phys. 04 (2016) 044.

[14] J. Ben Achour, M. Crisostomi, K. Koyama, D. Langlois, K. Noui, and G. Tasinato, J. High Energy Phys. 12 (2016) 100.

[15] H. Motohashi, K. Noui, T. Suyama, M. Yamaguchi, and D. Langlois, J. Cosmol. Astropart. Phys. 07 (2016) 033.

[16] J. Khoury, Classical Quantum Gravity **30**, 214004 (2013).

[17] C. Burrage, E. J. Copeland, A. Moss, and J. A. Stevenson, J. Cosmol. Astropart. Phys. 01 (2018) 056.

[18] P. Brax, C. van de Bruck, A.-C. Davis, and A. M. Green, Phys. Lett. B **633**, 441 (2006).

[19] P. Brax, C. van de Bruck, A.-C. Davis, J. Khoury, and A. Weltman, Phys. Rev. D **70**, 123518 (2004).

[20] P. Brax, A.-C. Davis, B. Li, H. A. Winther, and G.-B. Zhao, J. Cosmol. Astropart. Phys. 04 (2013) 029.

[21] N. Banerjee, S. Das, and K. Ganguly, Pramana **74**, L481 (2010).

[22] J. Khoury and A. Weltman, Phys. Rev. D **69**, 044026 (2004).

[23] T. Faulkner, M. Tegmark, E. F. Bunn, and Y. Mao, Phys. Rev. D **76**, 063505 (2007).

[24] I. Navarro and K. Van Acoleyen, J. Cosmol. Astropart. Phys. 02 (2007) 022.

[25] J. Khoury and A. Weltman, Phys. Rev. Lett. **93**, 171104 (2004).

[26] D. F. Mota and D. J. Shaw, Phys. Rev. D **75**, 063501 (2007).

[27] A. Terukina, L. Lombriser, K. Yamamoto, D. Bacon, K. Koyama, and R. C. Nichol, J. Cosmol. Astropart. Phys. 04 (2014) 013.

[28] A. Terukina and K. Yamamoto, Phys. Rev. D **86**, 103503 (2012).

[29] L. Lombriser, K. Koyama, and B. Li, J. Cosmol. Astropart. Phys. 03 (2014) 021.

[30] A. Tamosiunas, C. Briddon, C. Burrage, W. Cui, and A. Moss, J. Cosmol. Astropart. Phys. 04 (2022) 047.

[31] A. A. Starobinsky, JETP Lett. **86**, 157 (2007).

[32] H. Oyaizu, M. Lima, and W. Hu, Phys. Rev. D **78**, 123524 (2008).

[33] J. F. Navarro, C. S. Frenk, and S. D. M. White, Astrophys. J. **462**, 563 (1996).

[34] J. S. B. Wyithe, E. L. Turner, and D. N. Spergel, Astrophys. J. **555**, 504 (2001).

[35] J. Zavala, D. Nunez, R. A. Sussman, L. G. Cabral-Rosetti, and T. Matos, J. Cosmol. Astropart. Phys. 06 (2006) 008.

[36] T. Matos and D. Nunez, Rev. Mex. Fis. **51**, 71 (2005).

[37] R. Dehghani, P. Salucci, and H. Ghaffarnejad, Astron. Astrophys. **643**, A161 (2020).

[38] K. Asano, Publ. Astron. Soc. Jpn. **52**, 99 (2000).

[39] A. Terukina, L. Lombriser, K. Yamamoto, D. Bacon, K. Koyama, and R. C. Nichol, J. Cosmol. Astropart. Phys. 04 (2014) 013.

[40] S. Ettori, V. Ghirardini, D. Eckert, F. Dubath, and E. Pointecouteau, Mon. Not. R. Astron. Soc. **470**, L29 (2017).

[41] S. Ettori, V. Ghirardini, D. Eckert, E. Pointecouteau, F. Gastaldello, M. Sereno, M. Gaspari, S. Ghizzardi, M. Roncarelli, and M. Rossetti, Astron. Astrophys. **621**, A39 (2019).

[42] D. Eckert, S. Ettori, E. Pointecouteau, S. Molendi, S. Paltani, and C. Tchernin, Astron. Nachr. **338**, 293 (2017).

[43] V. Ghirardini et al., Astron. Astrophys. **621**, A41 (2019).

[44] P. A. R. Ade et al. (Planck Collaboration), Astron. Astrophys. **594**, A24 (2016).

[45] C. Arnold, E. Puchwein, and V. Springel, Mon. Not. R. Astron. Soc. **440**, 833 (2014).

[46] M. A. Mitchell, J.-h. He, C. Arnold, and B. Li, Mon. Not. R. Astron. Soc. **477**, 1133 (2018).

[47] M. A. Mitchell, C. Arnold, and B. Li, Mon. Not. R. Astron. Soc. **508**, 4157 (2021).

[48] H. A. Winther et al., Mon. Not. R. Astron. Soc. **454**, 4208 (2015).

[49] L. Lombriser, B. Li, K. Koyama, and G.-B. Zhao, Phys. Rev. D **87**, 123511 (2013).

[50] H. Wilcox et al., Mon. Not. R. Astron. Soc. **452**, 1171 (2015).

[51] R. Zaregonbadi, N. Saba, and M. Farhoudi, Eur. Phys. J. C **82**, 730 (2022).

[52] A. N. Ivanov and M. Wellenzohn, Universe **6**, 221 (2020).

[53] L. Kraiselburd, S. J. Landau, M. Salgado, D. Sudarsky, and H. Vucetich, Phys. Rev. D **97**, 104044 (2018).

[54] S. Tsujikawa, T. Tamaki, and R. Tavakol, J. Cosmol. Astropart. Phys. 05 (2009) 020.

[55] R. Kase and S. Tsujikawa, J. Cosmol. Astropart. Phys. 08 (2013) 054.

[56] M. Schaller, C. S. Frenk, R. G. Bower, T. Theuns, J. Trayford, R. A. Crain, M. Furlong, J. Schaye, C. Dalla Vecchia, and I. G. McCarthy, Mon. Not. R. Astron. Soc. **452**, 343 (2015).

[57] M. T. Hogan, B. R. McNamara, F. Pulido, P. E. J. Nulsen, H. R. Russell, A. N. Vantyghem, A. C. Edge, and R. A. Main, Astrophys. J. **837**, 51 (2017).

[58] B. Sartoris, A. Biviano, P. Rosati, A. Mercurio, C. Grillo, S. Ettori, M. Nonino, K. Umetsu, P. Bergamini, G. B. Caminha, and M. Girardi, Astron. Astrophys. **637**, A34 (2020).

[59] L. Lombriser, K. Koyama, G.-B. Zhao, and B. Li, Phys. Rev. D **85**, 124054 (2012).

[60] D. Shi, B. Li, J. Han, L. Gao, and W. A. Hellwing, Mon. Not. R. Astron. Soc. **452**, 3179 (2015).

[61] H. Wilcox, R. C. Nichol, G.-B. Zhao, D. Bacon, K. Koyama, and A. K. Romer, Mon. Not. R. Astron. Soc. **462**, 715 (2016).

[62] A. P. Naik, E. Puchwein, A.-C. Davis, D. Sijacki, and H. Desmond, Mon. Not. R. Astron. Soc. **489**, 771 (2019).

[63] L. Pizzuti, I. D. Saltas, and L. Amendola, Mon. Not. R. Astron. Soc. **506**, 595 (2021).

[64] B. Li and J. D. Barrow, Phys. Rev. D **83**, 024007 (2011).

[65] B. Li and G. Efstathiou, Mon. Not. R. Astron. Soc. **421**, 1431 (2012).

[66] B. Li and H. Zhao, Phys. Rev. D **81**, 104047 (2010).

[67] B. Jain, V. Vikram, and J. Sakstein, Astrophys. J. **779**, 39 (2013).

[68] H. A. Buchdahl, Mon. Not. R. Astron. Soc. **150**, 1 (1970).

[69] W. Hu and I. Sawicki, Phys. Rev. D **76**, 064004 (2007).

[70] P. Brax, C. van de Bruck, A.-C. Davis, and D. J. Shaw, Phys. Rev. D **78,** 104021 (2008).

[71] Y.-S. Song, W. Hu, and I. Sawicki, Phys. Rev. D **75,** 044004 (2007).

[72] L. Pizzuti, I. D. Saltas, A. Biviano, G. Mamon, and L. Amendola, J. Open Source Softwaare **8,** 4800 (2023).

[73] R. K. Jain, C. Kouvaris, and N. G. Nielsen, Phys. Rev. Lett. **116,** 151103 (2016).

[74] J. M. Z. Pretel, S. E. Jorás, and R. R. R. Reis, J. Cosmol. Astropart. Phys. 11 (2020) 048.

[75] M. Raveri, B. Hu, N. Frusciante, and A. Silvestri, Phys. Rev. D **90,** 043513 (2014).

[76] M. Cataneo, D. Rapetti, L. Lombriser, and B. Li, J. Cosmol. Astropart. Phys. 12 (2016) 024.

[77] L. Pizzuti, B. Sartoris, L. Amendola, S. Borgani, A. Biviano, K. Umetsu, A. Mercurio, P. Rosati, I. Balestra, G. B. Caminha, M. Girardi, C. Grillo, and M. Nonino, J. Cosmol. Astropart. Phys. 07 (2017) 023.

[78] E. L. D. Perico, R. Voivodic, M. Lima, and D. F. Mota, Astron. Astrophys. **632,** A52 (2019).

[79] X. Liu, B. Li, G.-B. Zhao, M.-C. Chiu, W. Fang, C. Pan, Q. Wang, W. Du, S. Yuan, L. Fu, and Z. Fan, Phys. Rev. Lett. **117,** 051101 (2016).

[80] H. Desmond and P. G. Ferreira, Phys. Rev. D **102,** 104060 (2020).

[81] L. Xu, Phys. Rev. D **91,** 063008 (2015).

[82] A. Vikhlinin, A. Kravtsov, W. Forman, C. Jones, M. Markevitch, S. S. Murray, and L. Van Speybroeck, Astrophys. J. **640,** 691 (2006).

[83] M. McDonald *et al.* (SPT Collaboration), Astrophys. J. **843,** 28 (2017).

[84] B. S. Haridasu, P. Karmakar, M. De Petris, V. F. Cardone, and R. Maoli, Phys. Rev. D **107,** 124059 (2023).

[85] B. S. Haridasu, P. Karmakar, M. De Petris, V. F. Cardone, and R. Maoli, EPJ Web Conf. **257,** 00021 (2022).

[86] P. Ade *et al.* (Planck Collaboration), Astron. Astrophys. **571,** A29 (2014).

[87] R. Herbonnet, C. Sifon, H. Hoekstra, Y. Bahe, R. F. J. van der Burg, J.-B. Melin, A. von der Linden, D. Sand, S. Kay, and D. Barnes, Mon. Not. R. Astron. Soc. **497,** 4684 (2020).

[88] D. Foreman-Mackey, D. W. Hogg, D. Lang, and J. Goodman, Publ. Astron. Soc. Pac. **125,** 306 (2013).

[89] D. W. Hogg and D. Foreman-Mackey, Astrophys. J. Suppl. Ser. **236,** 11 (2018).

[90] A. Lewis, arXiv:1910.13970.

[91] P. S. Corasaniti, C. Giocoli, and M. Baldi, Phys. Rev. D **102,** 043501 (2020).

[92] cosmosnet.it.

[93] web.infn.it/CSN4/IS/Linea5/InDark.

[94] A. A. Dutton and A. V. Macciò, Mon. Not. R. Astron. Soc. **441,** 3359 (2014).

[95] A. D. Ludlow, J. F. Navarro, R. E. Angulo, M. Boylan-Kolchin, V. Springel, C. Frenk, and S. D. M. White, Mon. Not. R. Astron. Soc. **441,** 378 (2014).

[96] P. Oleśkiewicz, C. M. Baugh, and A. Ludlow, Mon. Not. R. Astron. Soc. **489,** 4658 (2019).

[97] M. A. Mitchell, C. Hernández-Aguayo, C. Arnold, and B. Li, Mon. Not. R. Astron. Soc. **508,** 4140 (2021).